

1 Abstract

- 2 1. Accurate quantification of soil carbon fluxes is essential to reduce uncertainty in estimates
3 of the terrestrial carbon sink. However, these fluxes vary over time and across ecosystem
4 types and so it can be difficult to estimate them accurately across large scales. The flux
5 gradient method estimates soil carbon fluxes using co-located measurements of soil CO₂
6 concentration, soil temperature, soil moisture, and other soil properties. The National
7 Ecological Observatory Network (NEON) provides such data across 20 ecoclimatic domains
8 spanning the continental U.S., Puerto Rico, Alaska, and Hawai‘i.
- 9 2. We present an R software package (`neonSoilFlux`) that acquires soil environmental data
10 to compute half-hourly soil carbon fluxes for each soil replicate plot at a given terrestrial
11 NEON site. To assess the computed fluxes, we visited six focal NEON sites and measured
12 soil carbon fluxes using a closed-dynamic chamber approach.
- 13 3. Outputs from the `neonSoilFlux` showed agreement with measured fluxes (R^2 between
14 measured and `neonSoilFlux` outputs ranging from 0.12 to 0.77 depending on calculation
15 method used); measured outputs generally fell within the range of calculated uncertainties
16 from the gradient method. Calculated fluxes from `neonSoilFlux` aggregated to the daily
17 scale exhibited expected site-specific seasonal patterns.
- 18 4. While the flux gradient method is broadly effective, its accuracy is highly sensitive
19 to site-specific inputs, including the extent to which gap-filling techniques are used to
20 interpolate missing sensor data and to estimates of soil diffusivity and moisture content.
21 Future refinement and validation of `neonSoilFlux` outputs can contribute to existing
22 databases of soil carbon flux measurements, providing near real-time estimates of a critical
23 component of the terrestrial carbon cycle.

²⁴ **1.1 Keywords**

²⁵ Soil carbon, carbon dioxide, flux gradient, carbon cycle, field validation, soil respiration,
²⁶ ecosystem variability, diffusion

²⁷ **2 Introduction**

²⁸ Soils contain the planet's largest reservoir of terrestrial carbon (Jobbág & Jackson, 2000). A
²⁹ critical component of this reservoir is soil organic matter, the accumulation of which is influenced
³⁰ by biotic factors such as above-ground plant inputs (Jackson et al., 2017). These inputs in
³¹ turn are influenced by environmental factors such as growing season length, temperature, and
³² moisture (Desai et al., 2022), which also affect the breakdown of soil organic matter and its
³³ return to the atmosphere. Across heterogeneous terrestrial landscapes, the interplay between
³⁴ these biotic and abiotic factors influence the size of the soil contribution to the terrestrial
³⁵ carbon sink (Friedlingstein et al., 2025). However, the heterogeneity of these processes across
³⁶ diverse ecosystems in the context of rapid environmental change leads to large uncertainty
³⁷ about the magnitude of this sink in the future, and thus there remains a pressing need to
³⁸ quantify changes in soil carbon pools and fluxes across scales.

³⁹ Ecological observation networks such as the United States' National Ecological Observatory
⁴⁰ Network (NEON) and others (e.g. the globally-distributed FLUXNET or the European Inte-
⁴¹ grated Carbon Observation System) present a significant advancement in the nearly continuous
⁴² observation of biogeochemical processes at the continental scale. Notably, at 47 terrestrial
⁴³ sites across the continental United States that span 20 ecoclimatic domains, NEON provides
⁴⁴ half-hourly measurements of soil CO₂ concentration, temperature, and moisture at different
⁴⁵ vertical depths. Each of these NEON sites also encompasses measurements of the cumulative
⁴⁶ sum of all ecosystem carbon fluxes in an airshed using the eddy covariance technique (Baldocchi,

47 Soil observations provided by NEON are on the same timescale and standardized with
48 eddy covariance measurements from FLUXNET. These types of nearly continuous observational
49 data (NEON and FLUXNET) can be used to reconcile differences between model-derived
50 or data-estimated components of ecosystem carbon flux (Jian et al., 2022; Luo et al., 2011;
51 Phillips et al., 2017; J. Shao et al., 2015; P. Shao et al., 2013; Sihi et al., 2016).

52 Estimated or observed soil carbon fluxes are a key metric for understanding change in soil
53 carbon pools over time (Bond-Lamberty et al., 2024). A soil carbon flux to the atmosphere (F_S ,
54 units $\mu\text{mol m}^{-2} \text{s}^{-1}$), represents the aggregate process of transfer of soil CO_2 to the atmosphere
55 from physical and biological processes (e.g. diffusion and respiration). Soil carbon fluxes can
56 be assumed to encompass soil carbon respiration from autotrophic or heterotrophic sources
57 (Davidson et al., 2006) and modeled with a exponential Q_{10} paradigm (Bond-Lamberty et al.,
58 2004; Chen & Tian, 2005; Hamdi et al., 2013).

59 One common method by which F_S is measured in the field is through the use of soil chambers
60 in a closed, well-mixed system (Norman et al., 1997) with headspace trace gas concentrations
61 measured with an infrared gas analyzer (IRGA). F_S can also be estimated from soil CO_2
62 measurements at different depths in the soil using the flux-gradient method (Maier & Schack-
63 Kirchner, 2014). Closed-chamber IRGA measurements, while being the most common method,
64 require either frequent in-person site visits or expensive and fragile automated systems. The
65 potential of the gradient method is that fluxes can be estimated from continuous data recorded
66 by robust solid-state sensors. The flux-gradient method is an approach that uses conservation of
67 mass to calculate flux at a vertical soil depth z at steady state by applying Fick's law of diffusion.
68 A simplifying assumption for the flux-gradient method is that there is no mass transfer in the
69 other spatial dimensions x and y (Maier & Schack-Kirchner, 2014). The diffusivity profile, a
70 key component of this calculation, varies across the soil depth as a function of soil temperature,
71 soil volumetric water content, atmospheric air pressure, and soil bulk density (Millington &

72 Shearer, 1971; Moldrup et al., 1999; Sallam et al., 1984).

73 Databases such as the Soil Respiration Database (SRDB) or the Continuous Soil Respiration
74 Database (COSORE) add to the growing network of resources for making collected observations
75 of soil fluxes available to other researchers (Bond-Lamberty, 2018; Bond-Lamberty et al., 2020;
76 Bond-Lamberty & Thomson, 2010; Jian et al., 2021; Jiang et al., 2024). However, these
77 databases currently encompass primarily direct soil measurements of fluxes (i.e. those using
78 methods like the closed-chamber method described above). Currently, NEON provides all
79 measurements to calculate F_S from Fick's law, but soil flux as a derived data product was
80 descoped from the initial network launch due to budget constraints (Berenbaum et al., 2015).
81 Deriving estimates of F_S using continuous sensor data across NEON sites using NEON data
82 thus remains a high priority.

83 This study describes an R software package, `neonSoilFlux`, that computes a standardized
84 estimate of F_S at all terrestrial NEON sites using the flux-gradient method. Using direct
85 chamber-based field observations of soil carbon dioxide flux from a subset of terrestrial NEON
86 sites spanning six states, we provide a direct validation of F_S from `neonSoilFlux`. While
87 open source R software tools currently exist for processing chamber-based flux measurements
88 (Jurasinski et al., 2022; Pedersen, 2024; Rheault et al., 2024; Wilson et al., 2024; Zhao, 2019),
89 to our knowledge this is the first package that incorporates NEON data directly.

90 Key objectives of this study are to:

91 1. Apply the flux-gradient method to estimate soil CO₂ flux from continuous sensor mea-
92 surements across six NEON sites.
93 2. Benchmark estimated soil carbon fluxes against field measurements (e.g. direct chamber
94 measurements of soil flux).

- 95 3. Identify sources of error in the flux-gradient approach across diverse sites in order to
96 guide future work.

97 **3 Materials and Methods**

98 **3.1 Field methods**

99 **3.1.1 Focal NEON Sites**

100 In order to acquire field data to validate model predictions of flux, we selected six terrestrial
101 NEON sites for analysis. We conducted roughly week-long field measurement campaigns at
102 these sites, which span a range of environmental gradients and terrestrial domains (Table 1).
103 SJER, SRER, and WREF were visited during May and June of 2022, and WOOD, KONZ, and
104 UNDE during May and June of 2024. Permits or waivers were sought and approved prior to
105 field work at all six sites. In 2022, research activities were conducted whole or in part on the
106 Wind River Experimental Forest within the Gifford Pinchot National Forest. No permit was
107 required for this work. Approval for research at San Joaquin Experimental Range was granted
108 by Dr. Angela White in May 2022 and for research at Santa Rita Experimental Range by
109 Dr. Mitch McClaran in May 2022. In 2024, permits were received for work at WOOD (Chase
110 Lake WMD; permit number 62515-24-020), KONZ (Konza Prairie Biological Station; permit
111 number 766), and UNDE (University of Notre Dame Environmental Research Center; permit
112 number UNDERC-2024-5).

¹¹³ **3.1.2 Soil collar placement**

¹¹⁴ Either one (2022 sampling campaign) or two (2024 sampling campaign) PVC soil collars (20.1
¹¹⁵ cm inside diameter) were installed in close proximity to the permanent NEON soil sensors at
¹¹⁶ each site (Figure 1). As instruments in the NEON soil sensor arrays can occasionally break
¹¹⁷ down or stop working, the specific soil plot where we made measurements was chosen at each
¹¹⁸ site in consultation with NEON staff to maximize likelihood of quality soil sensor measurements
¹¹⁹ during the duration of the IRGA measurements. The plot selected at each site (out of the 5 in
¹²⁰ each replicate array at each site) are presented in the last column of Table 1. After installation,
¹²¹ collar(s) were left to equilibrate for approximately 24 hours prior to any measurements being
¹²² taken.

¹²³ **3.1.3 Infrared gas analyzer measurements of soil CO₂ flux**

¹²⁴ In 2022, we then made measurements of flux on an hourly interval for 8 hours each day.
¹²⁵ Measurements were taken from roughly 8 am to 4 pm, with the time interval selected to
¹²⁶ capture the majority of the diurnal gradient of soil temperature each day. These measurements
¹²⁷ were made using a LI-6800 infrared gas analyzer instrument (LI-COR Environmental, Lincoln,
¹²⁸ NE) fitted with a soil chamber attachment (attachment 6800-09). In 2024, we again used the
¹²⁹ same LI-6800 instrument, but made half-hourly measurements over an approximately 8 hour
¹³⁰ period. In addition, in 2024 we also installed a second collar and used a second instrument, an
¹³¹ LI-870 CO₂ IRGA, connected to an automated robotic chamber (LI-COR chamber 8200-104)
¹³² controlled by an LI-8250 multiplexer to make automated measurements. The multiplexer was
¹³³ configured to take half-hourly measurements 24 hours a day for the duration of our sampling
¹³⁴ bout at each site. Each instrument was paired with a soil temperature and moisture probe
¹³⁵ (Stevens HydraProbe, Stevens Water, Portland, OR) that was used to make soil temperature
¹³⁶ and moisture measurements concurrent with the CO₂ flux measurements. Chamber volumes

were set by measuring collar offsets at each site. System checks were conducted daily for the LI-6800 and weekly for the LI-8250. Instruments were factory calibrated before each field season.



Figure 1: Spatial layout of field sampling using a closed-dynamic chamber setup at a representative NEON site (KONZ). Left image shows collars (white arrows) and permanent soil sensor installation (black arrow) and right image shows the LI-6800 (foreground) and LI-8200-104 (background) instruments placed on the collars.

Table 1: Listing of NEON sites studied for field work and analysis. Site refers to NEON site codes: Santa Rita Experimental Range (SRER), San Joaquin Experimental Range (SJER), Wind River Experimental Forest (WREF), Chase Lake National Wildlife Refuge (WOOD), Konza Prairie Biological Station (KONZ), and the University of Notre Dame Environmental Research Center (UNDE). Location is reported in decimal degrees of latitude and longitude. Other abbreviations include Mean Annual Temperature (MAT); \bar{T}_S : average soil temperature during field measurements; \bar{SWC} : average soil water content during field measurements. Dates refer to field measurement dates for each site. Plot refers to the particular location in the soil sensor array (denoted as HOR by NEON) where field measurements were made.

Site	Location	Ecosystem	MAT	\bar{T}_S	MAP	\bar{SWC}	Dates	Plot
SRER	31.91068, -110.83549	Shrubland	19.3 °C	47.6 °C	346 mm	4.0%	May 29– June 1 2022	004
SJER	37.10878, -119.73228	Oak woodland	16.4 °C	41.7 °C	540 mm	1.2%	June 1–4 2022	005
WREF	45.82049, -121.95191	Evergreen forest	9.2 °C	15.3 °C	2225 mm	27.2%	June 7–9 2022	001

Table 1: Listing of NEON sites studied for field work and analysis. Site refers to NEON site codes: Santa Rita Experimental Range (SRER), San Joaquin Experimental Range (SJER), Wind River Experimental Forest (WREF), Chase Lake National Wildlife Refuge (WOOD), Konza Prairie Biological Station (KONZ), and the University of Notre Dame Environmental Research Center (UNDE). Location is reported in decimal degrees of latitude and longitude. Other abbreviations include Mean Annual Temperature (MAT); \bar{T}_S : average soil temperature during field measurements; \overline{SWC} : average soil water content during field measurements. Dates refer to field measurement dates for each site. Plot refers to the particular location in the soil sensor array (denoted as HOR by NEON) where field measurements were made.

Site	Location	Ecosystem	MAT	\bar{T}_S	MAP	\overline{SWC}	Dates	Plot
WOOD	47.1282, -99.241334	Restored prairie	4.9 °C	14.9 °C	495 mm	14.9%	June 3–9 2024	001
KONZ	39.100774, -96.563075	Tallgrass prairie	12.4 °C	23.4 °C	870 mm	23.4%	May 29– June 1 2024	001
UNDE	46.23391, -89.537254	Deciduous forest	4.3 °C	13.0 °C	802 mm	13.0%	May 22–25 2024	004

¹⁴⁰ 3.1.4 Post-collection processing of field data

¹⁴¹ We used LI-COR SoilFluxPro software (v 5.3.1) to assess the data after collection and to
¹⁴² inform sampling parameters. We checked appropriateness of dead band and measurement
¹⁴³ durations using built-in evaluation tools. Based on this, the deadband period was set for 30-40
¹⁴⁴ seconds, depending on the site, and the measurement duration was 180 seconds with a 30
¹⁴⁵ second pre-purge and a 30 second post-purge at most sites, and a 90 second pre- and post-purge
¹⁴⁶ at sites with higher humidity due to recent precipitation events. We also assessed the R^2 of
¹⁴⁷ linear and exponential model fits to measured CO₂ to verify measurement quality.

¹⁴⁸ 3.2 neonSoilFlux R package

¹⁴⁹ We developed an R package called `neonSoilFlux` (Zobitz et al., 2024) to compute half-hourly
¹⁵⁰ soil carbon fluxes and uncertainties from NEON data. The objective of the `neonSoilFlux`

151 package is a unified workflow (Figure 2) for soil data acquisition and analysis that supplements
152 the existing `neonUtilities` data acquisition R package (Lunch et al., 2025).

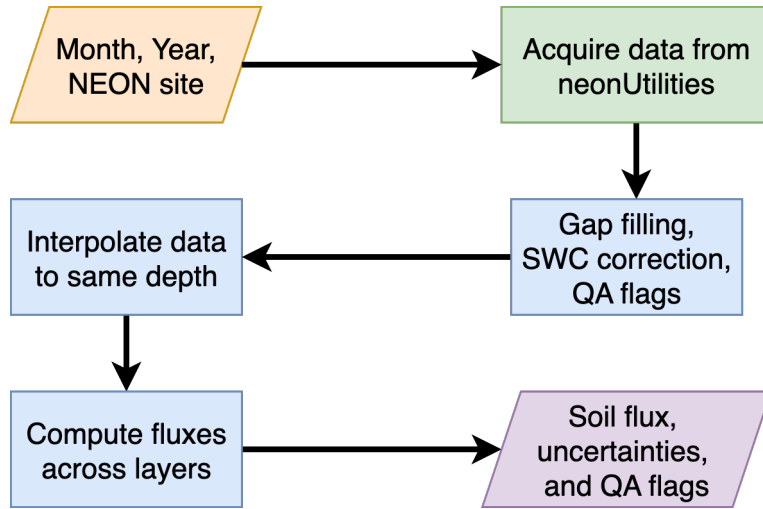


Figure 2: Diagram of `neonSoilFlux` R package. For a given month, year, and NEON site (orange parallelogram), the package acquires all relevant data to compute F_S using the `neonUtilities` R package (green rectangle). Data are gap-filled according to reported QA flags and adjusted for changes in soil water content (SWC) calibration coefficients, then interpolated to the same measurement depth before computing the soil flux, uncertainties, and final QA flags (blue rectangles). The package reports the associated soil flux, uncertainties, and quality assurance (QA) flags for the user (purple parallelogram).

153 At a given NEON site there are five replicate soil plots, each with measurements of soil
154 CO_2 concentration, soil temperature, and soil moisture at different depths (Figure 3). The
155 `neonSoilFlux` package acquires measured soil CO_2 concentration (NEON, 2024b), soil temper-
156 ature (NEON, 2024d), soil water content (NEON, 2024e), barometric pressure from the nearby
157 tower (NEON, 2024a), and soil properties (e.g. bulk density) (NEON, 2024c) from a range of
158 different NEON data products. The static soil properties were collected by NEON staff from a
159 nearby soil pit during initial site characterization and are assumed to be constant at each site.
160 A soil flux calculation is computed at each replicate soil plot.

161 The workflow to compute a value of F_S with `neonSoilFlux` consists of three primary steps,

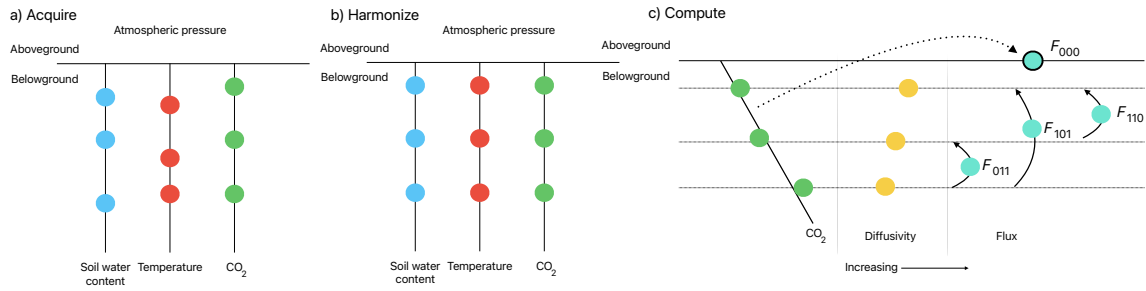


Figure 3: Model diagram of the data workflow for the `neonSoilFlux` R package. a) Acquire: Data are obtained for a given NEON location and horizontal sensor location, which includes soil water content, soil temperature, CO_2 concentration, and atmospheric pressure. All data are screened for quality assurance; if gap-filling of missing data occurs, it is flagged for the user. b) Harmonize: Any belowground data are then harmonized to the same depth as CO_2 concentrations using linear regression. c) Compute: The flux across a given depth is computed via Fick's law, denoted with F_{ijk} , where i , j , or k are either 0 or 1 denoting the layers the flux is computed across ($i =$ closest to surface, $k =$ deepest). F_{000} represents a flux estimate where the gradient dC/dz is the slope of a linear regression of CO_2 with depth.

illustrated in Figure 3. First, NEON data are acquired for a given site and month via the `neonUtilities` R package (yellow parallelogram and green rectangle in Figure 2 and Panel a in Figure 3). Acquired environmental data can be exported to a comma separated value file for additional analysis. Quality assurance (QA) flags are reported as an indicator variable. Since the calibration coefficients on the soil water content sensors have changed over time (NEON, 2024e), raw sensor measurements were back-calculated and soil-specific calibrations were applied following Ayres et al. (2024) to generate a consistent time series at each measurement location.

The second step is harmonizing the data to compute soil fluxes across soil layers. This step consists of three different actions (blue rectangles in Figure 2 and Panel b in Figure 3). If a given observation by NEON is reported as not passing a quality assurance check, we applied a gap filling method to replace that measurement with its monthly mean at that same depth (Section 3.2.1). Belowground measurements of soil water and soil temperature are then interpolated to the same depth as soil CO_2 measurements. The diffusivity (Section 3.2.2) and

175 soil flux across different soil layers (Section 3.2.3) are then computed.

176 The third and final step is computing a surface soil flux through extrapolation to the surface
177 (purple parallelogram in Figure 2 and Panel c in Figure 3). Uncertainty on a soil flux
178 measurement is computed through quadrature. An aggregate quality assurance (QA) flag for
179 each environmental measurement is also reported, representing if any gap-filled measurements
180 were used in the computation of a soil flux. Within the soil flux-gradient method, several
181 different approaches can be used to derive a surface flux (Maier & Schack-Kirchner, 2014); the
182 `neonSoilFlux` package reports four different possible values for soil surface flux (Section 3.2.3)
183 for each of two different methods of diffusivity estimation, for a total of eight estimates of
184 flux.

185 3.2.1 Gap-filling routine

186 NEON reports QA flags as binary values for each measurement and half-hourly interval. For a
187 given half-hour, if any input variable (soil CO₂ concentration, soil temperature, or soil moisture)
188 at depth z is flagged, computation of F_S is not possible. To address this, flagged measurements
189 and their uncertainties were replaced with a bootstrapped monthly mean (\bar{m}) and monthly
190 standard deviation (\bar{s}) (Efron & Tibshirani, 1994).

191 For each month, depth z , and variable, we computed bootstrapped estimates of \bar{m} and \bar{s}
192 from the vectors of unflagged measurements (**m**), reported standard errors (σ), and the 95%
193 confidence interval (ϵ , or expanded uncertainty; Farrance & Frenkel (2012)). We also defined a
194 bias vector $\mathbf{b} = \sqrt{\epsilon^2 - \sigma^2}$, which quantifies the spread of uncertainty in a given period and is
195 incorporated into \bar{m} .

196 From these, 5000 bootstrap samples were generated for **m**, σ , and **b**. For each sample (m_k, b_k, σ_k),
197 we generated a vector **n** (length $N = 5000$) by drawing from a normal distribution with mean

198 $m_k + b_k$ and standard deviation σ_k . The sample mean and standard deviation were then
199 computed from \mathbf{n} . The resulting distributions of sample means and sample standard deviations
200 provided the bootstrapped monthly mean (\bar{m}) and standard error (\bar{s}) respectively.

201 This gap-filling procedure provides a consistent treatment across all data streams. However,
202 alternative approaches may be better suited for longer gaps (e.g., correlations with other NEON
203 measurement levels or soil plots) or for variable-specific conditions. We discuss the effect of
204 gap-filling on our results in Section 5.1.

205 3.2.2 Soil diffusivity

206 Soil diffusivity D_a at a given measurement depth is the product of the diffusivity in free air
207 $D_{a,0}$ ($\text{m}^2 \text{ s}^{-1}$) and the tortuosity ξ (no units) (Millington & Shearer, 1971).

208 We compute $D_{a,0}$ with Equation 1:

$$D_{a,0} = 0.0000147 \cdot \left(\frac{T_i + 273.15}{293.15} \right)^{1.75} \cdot \left(\frac{P}{101.3} \right) \quad (1)$$

209 where T_i is soil temperature ($^\circ\text{C}$) at depth i (NEON, 2024d) and P surface barometric pressure
210 (kPa) (NEON, 2024a).

211 Previous studies by Sallam et al. (1984) and Tang et al. (2003) demonstrated the sensitivity
212 of modeled F_S depending on the tortuosity model (ξ) used to compute diffusivity. At low
213 soil water content, the choice of tortuosity model can lead to order-of-magnitude differences
214 in D_a , which in turn affect modeled F_S . The `neonSoilFlux` package currently includes two
215 approaches to calculate ξ , representing the range of tortuosity behavior reported in Sallam et
216 al. (1984).

217 The first approach is the Millington-Quirk model (Millington & Shearer, 1971), in which
218 tortuosity depends on both porosity and soil water content:

$$\xi = \frac{(\phi - SWC_i)^{10/3}}{\phi^2} \quad (2)$$

219 In Equation 2, SWC is the soil water content at depth i (NEON, 2024e) and ϕ is the porosity,
220 which in turn is a function of soil physical properties (NEON, 2024c):

$$\phi = \left(1 - \frac{\rho_s}{\rho_m}\right) (1 - f_V) \quad (3)$$

221 In Equation 3, ρ_m is the particle density of mineral soil (2.65 g cm^{-3}), ρ_s the soil bulk density
222 (g cm^{-3}) excluding coarse fragments greater than 2 mm (NEON, 2024c), and f_V is a site-specific
223 value that accounts for the proportion of soil fragments between 2-20 mm. Soil fragments
224 greater than 20 mm were not estimated due to limitations in the amount of soil that can be
225 analyzed (NEON, 2024c). We assume that rock fragments contain no internal pores.

226 The Millington-Quirk model assumes ξ is modulated by the amount of fluid saturation in soil
227 pores (Millington & Shearer, 1971). In contrast, the Marshall model (Marshall, 1959) expresses
228 tortuosity as only a function of porosity ($\xi = \phi^{1.5}$), with ϕ defined from Equation 3. The
229 Marshall model is independent of soil water content and assumes tortuosity is only governed
230 by soil structure. The `neonSoilFlux` package allows users to choose the tortuosity model most
231 appropriate for site-specific conditions and research goals.

232 **3.2.3 Soil flux computation**

233 We applied Fick's law (Equation 4) to compute the soil flux F_{ij} ($\mu\text{mol m}^{-2} \text{s}^{-1}$) across two soil
234 depths i and j :

$$F_{ij} = -D_a \frac{dC}{dz} \quad (4)$$

235 where D_a is the diffusivity ($\text{m}^2 \text{s}^{-1}$) and $\frac{dC}{dz}$ is the gradient of CO_2 molar concentration (μmol
236 m^{-3} , so the gradient has units of $\mu\text{mol m}^{-3} \text{m}^{-1}$). The soil surface flux is theoretically defined
237 by applying Equation 4 to measurements collected at the soil surface and directly below the
238 surface. Measurements of soil temperature, soil water content, and soil CO_2 molar concentration
239 across the soil profile allow for application of Equation 4 across different soil depths. Each
240 site had three measurement layers, so we denote the flux as a three-digit subscript F_{ijk} with
241 indicator variables i , j , and k indicate if a given layer was used (written in order of increasing
242 depth), according to the following:

- 243 • F_{000} is a surface flux estimate using the intercept of the linear regression of D_a with
244 depth and the slope from the linear regression of CO_2 with depth (which represents $\frac{dC}{dz}$
245 in Fick's Law). Tang et al. (2003) used this approach to compute fluxes in an oak-grass
246 savannah.
- 247 • F_{110} is a flux estimate across the two shallowest measurement layers.
- 248 • F_{011} is a flux estimate across the two deepest measurement layers.
- 249 • F_{101} is a flux estimate across the shallowest and deepest measurement layers.

250 For F_{110} , F_{011} , and F_{101} , the diffusivity used in Fick's Law is always at the deeper measurement
251 layer. When used as a surface flux estimate we assume CO_2 remains constant above this flux
252 depth. Uncertainty in all F_{ijk} values was quantified using quadrature (Taylor, 2022). These

253 computed fluxes could provide the basis for additional soil flux estimates. For example, Tang et
254 al. (2005) estimated surface flux by linearly extrapolating F_{110} and F_{011} to the soil surface.

255 **3.3 Post processing evaluation**

256 Following collection of field measurements and calculation of the soil fluxes from `neonSoilFlux`
257 package, we compared measured F_S based on closed-dynamic chamber measurements with the
258 LI-COR instruments to a given soil flux calculation from `neonSoilFlux` for each site and flux
259 computation method and quantified the relationship statistically (R^2). Finally, for a half-hourly
260 interval we also computed a *post hoc* diffusivity (D_a) using the LI-COR flux along with the
261 CO_2 surface gradient reported by NEON using the measurement levels closest to the surface.

262 **4 Results**

263 **4.1 Concordance between modelled and measured soil CO_2 flux**

264 The sites we visited ranged substantially in both their annual average temperature and
265 precipitation as well as their biome type (Table 2). These differences also influenced the wide
266 range of observed flux rates across sites.

267 The timeseries of the measured fluxes from the LI-COR 6800 and 870/8250 were compared
268 to modeled soil fluxes from the `neonSoilFlux` R package (Figure 4). We also assessed year-
269 long estimated flux time series and compared those to field measurements made at each site
270 (Figure 5). Results are reported in local time. Where applicable, sites are displayed from left
271 to right by increasing soil temperature (Table 1). Positive values of the flux indicate that there
272 is a flux moving towards the surface. Overall, with the exception of SRER (discussed later) the
273 computed fluxes determined using a variety of plausible methods spanned the field-measured

Table 2: Summary of measured soil characteristics and flux results from field measurements across six NEON sites using a LI-COR 6800 (LI-870/8250 measurements omitted to enable direct comparability) via the closed-dynamic chamber method. Numeric values for soil CO₂ flux, soil temperature, and volumetric soil water content (VSWC) are the mean and standard deviation of field measurements at each site.

Site	Flux μmol m ⁻² s ⁻¹	Soil temp °C	VSWC cm ³ cm ⁻³	n
UNDE	2.55 ± 0.26	14.33 ± 0.77	0.33 ± 0.02	61
WOOD	3.02 ± 0.4	16.01 ± 1.54	0.28 ± 0.01	53
WREF	3.62 ± 0.3	15.34 ± 1.76	0.27 ± 0.06	21
KONZ	6.35 ± 0.97	27.28 ± 4.14	0.37 ± 0.01	44
SJER	0.94 ± 0.02	41.68 ± 11.22	0.01 ± 0.01	32
SRER	0.72 ± 0.09	47.64 ± 7.46	0.04 ± 0.01	32

²⁷⁴ fluxes, but the specific flux-gradient method that best approximated field measurements varied
²⁷⁵ by site.

²⁷⁶ We calculated a statistical relationship between the various estimates of soil flux computed by
²⁷⁷ `neonSoilFlux` and the field-measured fluxes within daily interval periods. Statistics for these
²⁷⁸ comparisons are reported in Figure 6, which also shows how these fall relative to a 1:1 line.

²⁷⁹ 4.2 Effects of method choice on diffusivity estimates

²⁸⁰ In one of the six field sites, the *post hoc* D_a estimate fell roughly between the two diffusion
²⁸¹ estimation methods. At UNDE, WOOD, WREF, and SJER, the median field estimate of
²⁸² diffusivity was lower than both of the other methods. At the driest sites, SRER (Table 1),
²⁸³ the median field estimate of diffusivity was higher than both of the other methods and values
²⁸⁴ showed a large amount of variation (Figure 7).

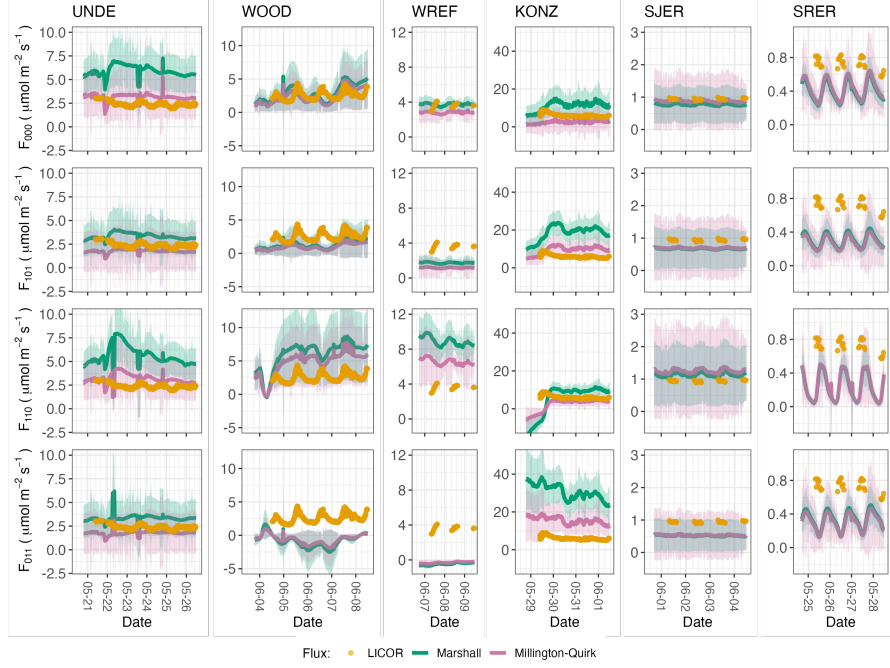


Figure 4: Timeseries of soil surface flux (F_S) from field-measured (yellow lines) and modeled soil fluxes (green or purple lines) by the `neonSoilFlux` R package. Fluxes from the `neonSoilFlux` R package are separated by the diffusivity model used (Millington-Quirk or Marshall, Section 3.2.2). Individual vertical axis labels in the first column represent the measurement levels where the flux-gradient approach is applied (Section 3.2.3). Ribbons for modeled soil fluxes represent approximately ± 1 standard deviation. Results are reported in local time. WREF, SJER, and SRER were sampled in 2022, and UNDE, WOOD, and KONZ were sampled in 2024. Sites (columns) are arranged from left to right in terms of increasing mean annual temperature.

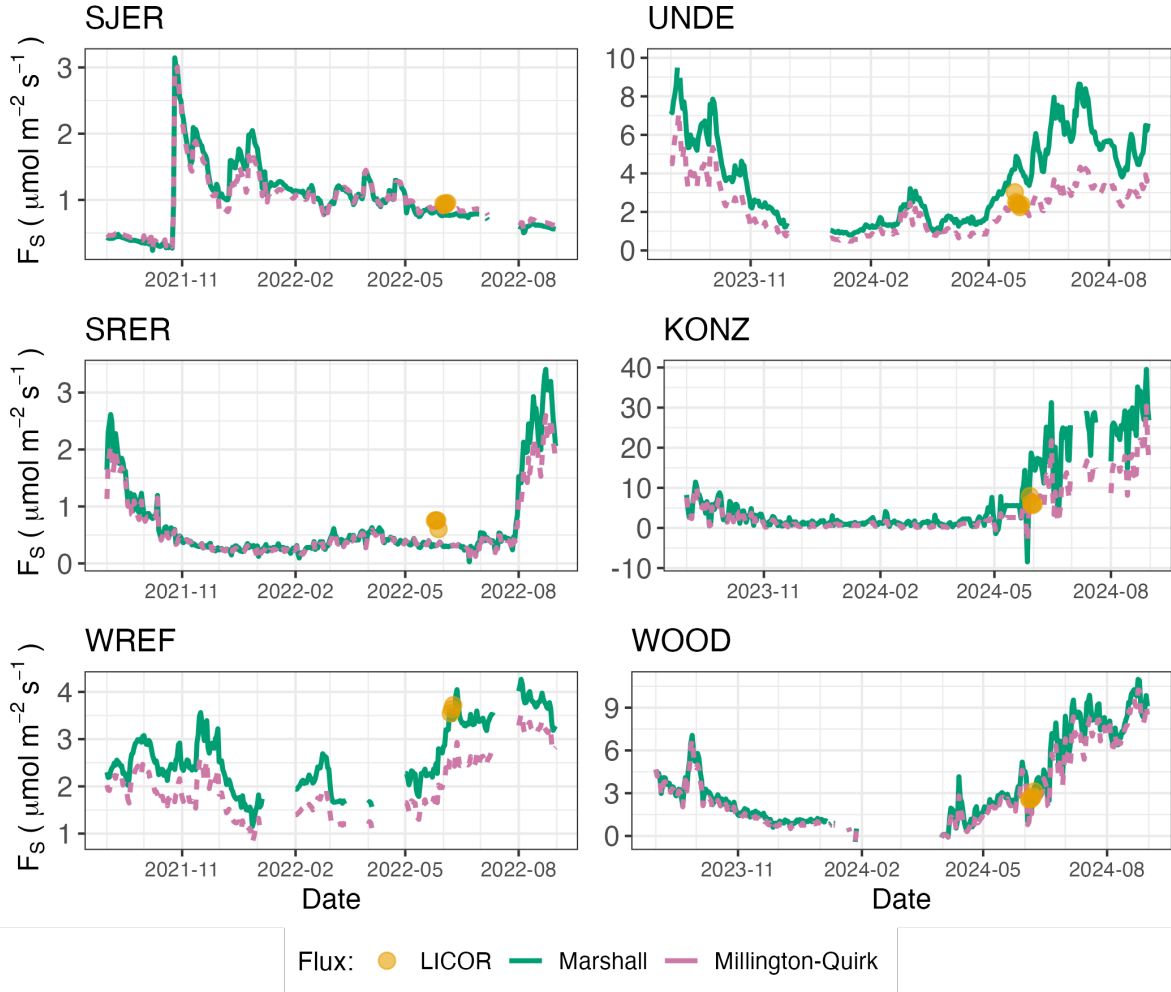


Figure 5: Timeseries of both daily-averaged field F_S (yellow circles) and daily ensemble averaged soil fluxes (average of F_{000} , F_{101} , F_{011} , F_{110} , Section 3.2.3) by the `neonSoilFlux` R package, separated by the diffusivity model used (green or purple lines, Millington-Quirk or Marshall, Section 3.2.2).

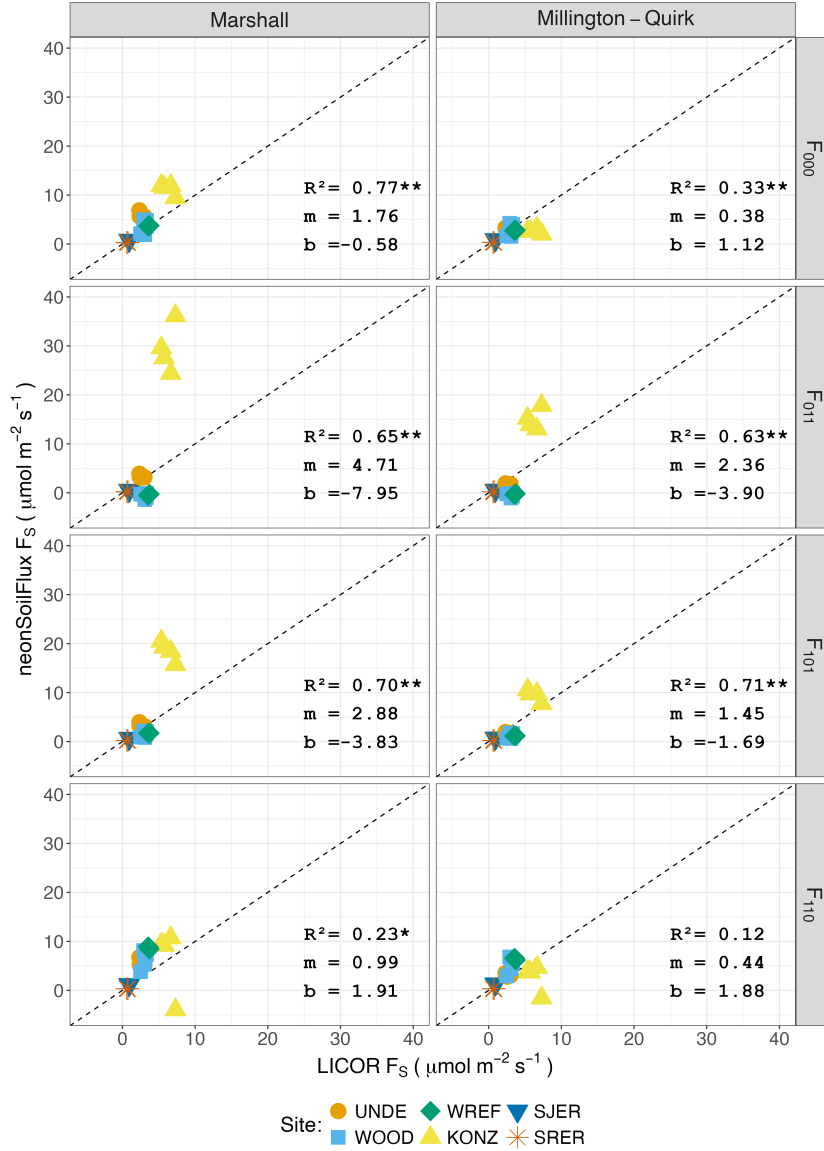


Figure 6: Statistical comparison between measured fluxes at each NEON site with fluxes reported by `neonSoilFlux` with the different flux calculation approaches and diffusivity calculations applied. Points are daily averages and LICOR F_S values are from the 6800 instrument only, for consistency. The dotted line represents a 1:1 relationship, and the reported R^2 quantifies the relationship between field-measured and `neonSoilFlux` estimated fluxes. * = significance at the 5% level, ** = significance at the 1% level. The slope (m) and intercept (b) of the linear regression between measured and modeled fluxes are also reported. The low-value outlier from KONZ in the F_{110} Marshall plot is an example of the effect of inverted CO₂ gradients causing an estimated flux to be negative, bringing down the daily mean, which later resolved as the soils dried back out.

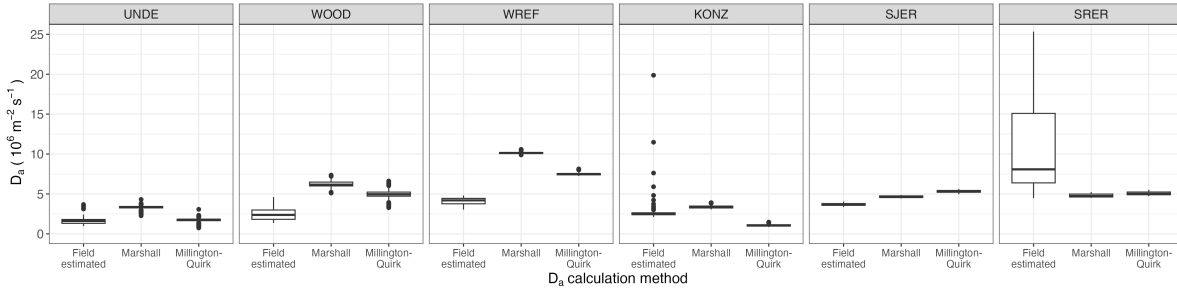


Figure 7: Distribution of diffusivity (D_a) at each study site. Values of D_a were provided by the `neonSoilFlux` package, computed from the Millington-Quirk or Marshall models (Section 3.2.2). A post-hoc estimate of diffusivity (labeled as “Field estimated”) was computed through the field measured flux (Figure 4), divided by the CO₂ gradient from the measurement levels closest to the soil surface, as reported by NEON. We only used F_S measured by the LICOR 6800 at all sites to standardize comparisons. Some outliers ($n = 1$ from the field estimated values at KONZ and $n = 6$ from field estimated values at SRER) are excluded from the plot to allow better comparative visualization across sites.

285 5 Discussion

286 This study presents a unified data science workflow to efficiently process automated measurements of belowground soil CO₂ concentrations, soil water content, and soil temperature to
 287 infer estimates of soil surface CO₂ effluxes through application of Fick’s Law (Equation 4).
 288 Our core goals in this study were: (1) to generate estimates of soil flux from continuous soil
 289 sensor data at terrestrial NEON sites using the flux-gradient method and then (2) to compare
 290 those estimates to field-measured fluxes based on the closed chamber approach at six NEON
 291 focal sites. We discuss our progress toward these core goals through (1) an overall evaluation
 292 of the flux-gradient approach (and uncertainty calculation) and (2) site-specific evaluation of
 293 differences in estimated vs measured fluxes.
 294

295 **5.1 General evaluation of flux-gradient approach**

296 Key assumptions of the flux-gradient approach are that CO₂ concentrations increase throughout
297 the soil profile such that the highest concentrations are observed in the deepest layers. Addition-
298 ally, field flux measurements should correlate with F_{000} because they represent surface fluxes.
299 Periods where this gradient condition are not met generally are connected to processes that occur
300 during soil wetting events, where more shallow soil layers produce higher concentrations of CO₂
301 due to microbial respiration pulses following rewetting. This effect is likely to be largest at sites
302 with rich organic soils (e.g. KONZ). Based on this reasoning, in these types of situations we would
303 *a priori* expect F_{011} (deepest layers) $\leq F_{101} \leq F_{110}$ (shallow layers) $\leq F_{000}$ (all layers) be-
304 cause the previous flux estimates rely primarily on CO₂ concentrations at deeper depths, and
305 could miss high concentrations of CO₂ produced in shallower layers.

306 When modeling soil respiration, typically a non-linear response function that also considers soil
307 type is used (Bouma & Bryla, 2000; Yan et al., 2016, 2018). For the `neonSoilFlux` package,
308 soil type is connected to the measurement of bulk density, which was characterized at each
309 NEON site. This bulk density estimate is based on replicate samples collected from the site
310 megapit at a subset of soil horizons, with an estimated uncertainty of $\pm 5\%$ (NEON, 2024c).
311 Coarse fragment estimates also have very large uncertainties, but because the volume fraction
312 tends to be low in surface soils it is unlikely to contribute much additional flux uncertainty.

313 Our results suggest that the most important way to improve reliability of the flux estimate is
314 to reduce the usage of gap-filled data. The current approach to gap filling in `neonSoilFlux`
315 uses monthly mean data to gap fill—this approach decreases the ability of the estimate to
316 be responsive to short-term pulses that occur with rapid weather shifts. All sites had more
317 than 75% of half-hourly periods with no-gap filled measurements (Figure S1, Supplementary
318 Information). At five out of six sites (all except SRER), we used at least some gap-filled
319 measurements of Soil Water Content (SWC). At WREF, field data collection occurred following

320 a severe rainstorm, with soils at the beginning of the sampling week near their water holding
321 capacity, which can influence the soil moisture sensor accuracy. In general, we recommend that
322 whenever possible, knowledge of local field conditions should influence analysis decisions in
323 addition to any QA filtering protocols in the `neonSoilFlux` package.

324 We recognize that this gap-filling approach may lead to gap-filled values that are quite different
325 from the actual values, such as an underestimate of soil moisture following rain events. Further
326 extensions of the gap filling method could use more sophisticated gap-filling routines, similar to
327 what is used for net ecosystem carbon exchange (Falge et al., 2001; Liu et al., 2023; Mariethoz
328 et al., 2015; Moffat et al., 2007; Zhang et al., 2023). Additionally, since the deepest temperature
329 and soil moisture sensors are located below the deepest CO₂ sensors at NEON sites, it is
330 possible that excluding these deeper layers from consideration prior to analysis would lead to a
331 reduced need for gap filling. Future iterations of the `neonSoilFlux` package may incorporate
332 this as an option. The current gap-filling routine provides a consistent approach that can be
333 applied to each data stream, but further work may explore alternative gap-filling approaches.

334 **5.2 Evaluation of flux-gradient approach at each site**

335 Derived results from the `neonSoilFlux` package have patterns that are broadly consistent with
336 those directly measured in the field (Figure 4 and Figure 5), even though statistical comparisons
337 between the field-measured and `neonSoilFlux` values were quite variable (e.g. R^2 ranging
338 from 0.12 to 0.77; Figure 6). One advantage of the `neonSoilFlux` package is its ability to
339 calculate fluxes across different soil depths (Figure 3), which allows for additional site-specific
340 customization. We believe the package can provide a useful baseline estimate of soil fluxes that
341 can always be complemented through additional field measurements.

342 The six locations studied provide a range of case studies that suggest different considerations

may apply to different sites when applying the flux-gradient method. For example, the Santa Rita Experimental Range (SRER) is a desert site characterized by sandy soil, which also was the location of the highest field soil temperatures that we observed (Table 2). At SRER the flux across the top two layers (F_{110}) produced a pattern of soil flux most consistent with the observed field data. The remaining methods F_{101} , F_{011} , or F_{000} are derived from information taken from the deepest layer, which seems to have been decoupled from the surface layers both in terms of temperature and CO₂ concentration. This may be a general circumstance where there are large diurnal temperature extremes that rapidly change during the course of a day and overnight, leading to lags in the timing of when temperature increases propagate down to deeper soil layers.

Immediately prior to our visit to Konza Prairie (KONZ), that site that experienced a significant rain event that led to wet soils that gradually dried out over the course of our time there. This pulse of precipitation increased the soil CO₂ concentration at the top layer above the concentrations in lower layers, leading to negative estimated flux values at the start of the field sampling period. In this case it was only when the soil began to return to a baseline level that the assumptions of the flux-gradient method were again met.

Both of the previous cases also provide context for the variable statistical comparisons between field-measured soil fluxes and `neonSoilFlux` outputs (Figure 6). When considering systematic deployment of this method across a measurement network, there are a number of independent challenges that require careful consideration. There are clear tradeoffs between (1) accuracy of modeled fluxes (defined here as closeness to field-measured F_S and the uncertainty reduction factor ϵ), (2) precision (which could be defined by the signal to noise ratio), and (3) the choice of the diffusivity model (Section 3.2.2) or flux computation method (Section 3.2.3). We performed a sensitivity analysis to compare the impact of these factors (Figure S2, Supplemental Information).

Finally, comparing the effects of different diffusivity estimation methods on the match between modeled and measured fluxes (Figure 5) highlights the sensitivity of F_{ijk} to diffusivity. The comparison between diffusivity estimates compared to field estimated diffusivity (Figure 7) demonstrates that site parameters can dictate which measure of diffusivity is most likely to be accurate in a given environmental context. Site-specific differences are largely a reflection of differences in soil moisture across the sites (Table 1), as not all diffusivity estimation methods incorporate soil moisture equivalently. While we here have compares two approaches to calculate diffusivity (the Millington-Quirk and Marshall models), it may be valuable to evaluate other diffusivity models (e.g. the Moldrup model; Moldrup et al. (1999)) as well. Ultimately the choice of a particular diffusivity model could be determined based on knowledge of site-specific evaluations or a set of these models could be used to generate a model ensemble average as a means to trade precision for a more general approach.

5.3 Recommendations for future method development

The `neonSoilFlux` package provides several approaches to estimate soil flux using the gradient method. We believe these approaches enable the software to be used across a range of site-specific assumptions (Maier & Schack-Kirchner, 2014). We note, however, that this choice can have a determinative approach on the calculated values. Ensemble averaging approaches (Elshall et al., 2018; Raftery et al., 2005) may be one way to address this problem if the goal is to calculate fluxes using the same method at a diverse range of different sites. Two other ideas would be to apply machine learning algorithms (*e.g.* random forest) to generate a single flux estimate across diverse sites, or using co-located estimates of net ecosystem carbon exchange from eddy-flux towers to further constrain results or to assess soil flux results for plausibility (Phillips et al., 2017).

These challenges notwithstanding, the method used here and made available in the

392 `neonSoilFlux` R package has the potential to produce nearly continuous estimates of flux
393 across all terrestrial NEON sites. These estimates are a significant improvement on available
394 approaches to constrain the portion of ecosystem respiration attributable to the soil. This, in
395 turn, also aids in our ability to understand the soil contribution to the net ecosystem flux
396 measured at these sites using the co-located eddy flux towers.

397 **6 Conclusions**

398 We used the R package `neonSoilFlux` to estimate soil CO₂ fluxes with the flux-gradient method
399 using data from buried soil sensors at NEON terrestrial sites. We compared the predicted
400 fluxes to those measured directly using a field-based closed chamber approach. Soil fluxes
401 from `neonSoilFlux` were broadly effective at producing estimates of flux comparable to those
402 measured in the field using a chamber-based technique. However `neonSoilFlux` outputs are
403 quite sensitive to a number of issues, including: missing data (and thus gap-filling of input
404 measurement datasets), the selection of soil depths used to best calculate the gradient (which
405 may vary between sites), and finally the choice of method used for estimating soil diffusivity.
406 The flexibility of the `neonSoilFlux` package allows the user to evaluate each of these issues
407 with site-specific knowledge and contexts. Future refinements and subsequent validation of
408 `neonSoilFlux` outputs will feed forward into evaluating soil carbon fluxes broader spatial scales
409 to enhance understanding of the ways in which soils across diverse ecosystems are responding
410 to a changing climate.

⁴¹¹ **Sources Cited**

- ⁴¹² Ayres, E., Reichle, R. H., Colliander, A., Cosh, M. H., & Smith, L. (2024). Validation of
⁴¹³ Remotely Sensed and Modeled Soil Moisture at Forested and Unforested NEON Sites.
⁴¹⁴ *IEEE Journal of Selected Topics in Applied Earth Observations and Remote Sensing*, 17,
⁴¹⁵ 14248–14264. <https://doi.org/10.1109/JSTARS.2024.3430928>
- ⁴¹⁶ Baldocchi, D. (2014). Measuring fluxes of trace gases and energy between ecosystems and the
⁴¹⁷ atmosphere - the state and future of the eddy covariance method. *Global Change Biology*,
⁴¹⁸ 20(12), 3600–3609. <https://doi.org/10.1111/gcb.12649>
- ⁴¹⁹ Berenbaum, M. R., Carpenter, S. R., Hampton, S. E., Running, S. W., & Stanzione, D. C.
⁴²⁰ (2015). *Report from the NSF BIO Advisory Committee Subcommittee on NEON Scope
421 Impacts*.
- ⁴²² Bond-Lamberty, B. (2018). New Techniques and Data for Understanding the Global Soil
⁴²³ Respiration Flux. *Earth's Future*, 6(9), 1176–1180. <https://doi.org/10.1029/2018EF000866>
- ⁴²⁴ Bond-Lamberty, B., Ballantyne, A., Berryman, E., Fluet-Chouinard, E., Jian, J., Morris, K.
⁴²⁵ A., Rey, A., & Vargas, R. (2024). Twenty Years of Progress, Challenges, and Opportunities
⁴²⁶ in Measuring and Understanding Soil Respiration. *Journal of Geophysical Research: Biogeosciences*, 129(2), e2023JG007637. <https://doi.org/10.1029/2023JG007637>
- ⁴²⁸ Bond-Lamberty, B., Christianson, D. S., Malhotra, A., Pennington, S. C., Sihi, D., AghaK-
⁴²⁹ ouchak, A., Anjileli, H., Altaf Arain, M., Armesto, J. J., Ashraf, S., Ataka, M., Baldocchi,
⁴³⁰ D., Andrew Black, T., Buchmann, N., Carbone, M. S., Chang, S.-C., Crill, P., Curtis, P.
⁴³¹ S., Davidson, E. A., ... Zou, J. (2020). COSORE: A community database for continuous
⁴³² soil respiration and other soil-atmosphere greenhouse gas flux data. *Global Change Biology*,
⁴³³ 26(12), 7268–7283. <https://doi.org/10.1111/gcb.15353>
- ⁴³⁴ Bond-Lamberty, B., & Thomson, A. (2010). A global database of soil respiration data.
⁴³⁵ *Biogeosciences*, 7(6), 1915–1926. <https://doi.org/10.5194/bg-7-1915-2010>

- 436 Bond-Lamberty, B., Wang, C., & Gower, S. T. (2004). A global relationship between the
437 heterotrophic and autotrophic components of soil respiration? *Global Change Biology*,
438 10(10), 1756–1766. <https://doi.org/10.1111/j.1365-2486.2004.00816.x>
- 439 Bouma, T. J., & Bryla, D. R. (2000). On the assessment of root and soil respiration for soils of
440 different textures: Interactions with soil moisture contents and soil CO₂ concentrations.
441 *Plant and Soil*, 227(1), 215–221. <https://doi.org/10.1023/A:1026502414977>
- 442 Chen, H., & Tian, H.-Q. (2005). Does a General Temperature-Dependent Q10 Model of Soil
443 Respiration Exist at Biome and Global Scale? *Journal of Integrative Plant Biology*, 47(11),
444 1288–1302. <https://doi.org/10.1111/j.1744-7909.2005.00211.x>
- 445 Davidson, E. A., Janssens, I. A., & Luo, Y. (2006). On the variability of respiration in
446 terrestrial ecosystems: Moving beyond Q10. *Global Change Biology*, 12, 154–164. <https://doi.org/10.1111/j.1365-2486.2005.01065.x>
- 447
- 448 Desai, A. R., Murphy, B. A., Wiesner, S., Thom, J., Butterworth, B. J., Koupaei-Abyazani, N.,
449 Muttaqin, A., Paleri, S., Talib, A., Turner, J., Mineau, J., Merrelli, A., Stoy, P., & Davis,
450 K. (2022). Drivers of Decadal Carbon Fluxes Across Temperate Ecosystems. *Journal of
451 Geophysical Research: Biogeosciences*, 127(12), e2022JG007014. <https://doi.org/10.1029/2022JG007014>
- 452
- 453 Efron, B., & Tibshirani, R. J. (1994). *An Introduction to the Bootstrap*. Chapman and
454 Hall/CRC. <https://doi.org/10.1201/9780429246593>
- 455 Elshall, A. S., Ye, M., Pei, Y., Zhang, F., Niu, G.-Y., & Barron-Gafford, G. A. (2018). Relative
456 model score: A scoring rule for evaluating ensemble simulations with application to microbial
457 soil respiration modeling. *Stochastic Environmental Research and Risk Assessment*, 32(10),
458 2809–2819. <https://doi.org/10.1007/s00477-018-1592-3>
- 459 Falge, E., Baldocchi, D., Olson, R., Anthoni, P., Aubinet, M., Bernhofer, C., Burba, G.,
460 Ceulemans, R., Clement, R., Dolman, H., Granier, A., Gross, P., Grünwald, T., Hollinger,
461 D., Jensen, N.-O., Katul, G., Keronen, P., Kowalski, A., Lai, C. T., ... Wofsy, S. (2001).

- 462 Gap filling strategies for defensible annual sums of net ecosystem exchange. *Agricultural*
463 *and Forest Meteorology*, 107(1), 43–69. [https://doi.org/10.1016/S0168-1923\(00\)00225-2](https://doi.org/10.1016/S0168-1923(00)00225-2)
- 464 Farrance, I., & Frenkel, R. (2012). *Uncertainty of Measurement: A Review of the Rules*
465 *for Calculating Uncertainty Components through Functional Relationships*. *The Clinical*
466 *Biochemist Reviews*, 33(2), 49–75.
- 467 Friedlingstein, P., O’Sullivan, M., Jones, M. W., Andrew, R. M., Hauck, J., Landschützer,
468 P., Le Quéré, C., Li, H., Luijkh, I. T., Olsen, A., Peters, G. P., Peters, W., Pongratz,
469 J., Schwingshackl, C., Sitch, S., Canadell, J. G., Ciais, P., Jackson, R. B., Alin, S. R., ...
470 Zeng, J. (2025). Global Carbon Budget 2024. *Earth System Science Data*, 17(3), 965–1039.
471 <https://doi.org/10.5194/essd-17-965-2025>
- 472 Hamdi, S., Moyano, F., Sall, S., Bernoux, M., & Chevallier, T. (2013). Synthesis analysis
473 of the temperature sensitivity of soil respiration from laboratory studies in relation to
474 incubation methods and soil conditions. *Soil Biology and Biochemistry*, 58, 115–126.
475 <https://doi.org/10.1016/j.soilbio.2012.11.012>
- 476 Jackson, R. B., Lajtha, K., Crow, S. E., Hugelius, G., Kramer, M. G., & Piñeiro, G. (2017).
477 The Ecology of Soil Carbon: Pools, Vulnerabilities, and Biotic and Abiotic Controls.
478 *Annual Review of Ecology, Evolution and Systematics*, 48(Volume 48, 2017), 419–445.
479 <https://doi.org/10.1146/annurev-ecolsys-112414-054234>
- 480 Jian, J., Bailey, V., Dorheim, K., Konings, A. G., Hao, D., Shiklomanov, A. N., Snyder,
481 A., Steele, M., Teramoto, M., Vargas, R., & Bond-Lamberty, B. (2022). Historically
482 inconsistent productivity and respiration fluxes in the global terrestrial carbon cycle. *Nature*
483 *Communications*, 13(1), 1733. <https://doi.org/10.1038/s41467-022-29391-5>
- 484 Jian, J., Vargas, R., Anderson-Teixeira, K., Stell, E., Herrmann, V., Horn, M., Kholod, N.,
485 Manzon, J., Marchesi, R., Paredes, D., & Bond-Lamberty, B. (2021). A restructured and
486 updated global soil respiration database (SRDB-V5). *Earth System Science Data*, 13(2),
487 255–267. <https://doi.org/10.5194/essd-13-255-2021>

- 488 Jiang, J., Feng, L., Hu, J., Liu, H., Zhu, C., Chen, B., & Chen, T. (2024). Global soil
489 respiration predictions with associated uncertainties from different spatio-temporal data
490 subsets. *Ecological Informatics*, 82, 102777. <https://doi.org/10.1016/j.ecoinf.2024.102777>
- 491 Jobbágy, E. G., & Jackson, R. B. (2000). The Vertical Distribution of Soil Organic Carbon
492 and its Relation to Climate and Vegetation. *Ecological Applications*, 10(2), 423–436.
493 [https://doi.org/10.1890/1051-0761\(2000\)010%5B0423:TVDOSO%5D2.0.CO;2](https://doi.org/10.1890/1051-0761(2000)010%5B0423:TVDOSO%5D2.0.CO;2)
- 494 Jurasinski, G., Koebisch, F., Guenther, A., & Beetz, S. (2022). *Flux: Flux Rate Calculation
495 from Dynamic Closed Chamber Measurements*.
- 496 Liu, K., Li, X., Wang, S., & Zhang, H. (2023). A robust gap-filling approach for European
497 Space Agency Climate Change Initiative (ESA CCI) soil moisture integrating satellite
498 observations, model-driven knowledge, and spatiotemporal machine learning. *Hydrology
499 and Earth System Sciences*, 27(2), 577–598. <https://doi.org/10.5194/hess-27-577-2023>
- 500 Lunch, C., Laney, C., Mietkiewicz, N., Sokol, E., Cawley, K., & Network), N. (National. E. O.
501 (2025). *neonUtilities: Utilities for Working with NEON Data*.
- 502 Luo, Y., Ogle, K., Tucker, C., Fei, S., Gao, C., LaDeau, S., Clark, J. S., & Schimel, D. S. (2011).
503 Ecological forecasting and data assimilation in a data-rich era. *Ecological Applications*,
504 21(5), 1429–1442. <https://doi.org/10.1890/09-1275.1>
- 505 Maier, M., & Schack-Kirchner, H. (2014). Using the gradient method to determine soil gas
506 flux: A review. *Agricultural and Forest Meteorology*, 192–193, 78–95. <https://doi.org/10.1016/j.agrformet.2014.03.006>
- 508 Mariethoz, G., Linde, N., Jougnot, D., & Rezaee, H. (2015). Feature-preserving interpolation
509 and filtering of environmental time series. *Environmental Modelling & Software*, 72, 71–76.
510 <https://doi.org/10.1016/j.envsoft.2015.07.001>
- 511 Marshall, T. J. (1959). The Diffusion of Gases Through Porous Media. *Journal of Soil Science*,
512 10(1), 79–82. <https://doi.org/10.1111/j.1365-2389.1959.tb00667.x>
- 513 Millington, R. J., & Shearer, R. C. (1971). Diffusion in aggregated porous media. *Soil Science*,

- 514 111(6), 372–378.
- 515 Moffat, A. M., Papale, D., Reichstein, M., Hollinger, D. Y., Richardson, A. D., Barr, A. G.,
516 Beckstein, C., Braswell, B. H., Churkina, G., Desai, A. R., Falge, E., Gove, J. H., Heimann,
517 M., Hui, D., Jarvis, A. J., Kattge, J., Noormets, A., & Stauch, V. J. (2007). Comprehensive
518 comparison of gap-filling techniques for eddy covariance net carbon fluxes. *Agricultural and*
519 *Forest Meteorology*, 147(3), 209–232. <https://doi.org/10.1016/j.agrformet.2007.08.011>
- 520 Moldrup, P., Olesen, T., Yamaguchi, T., Schjønning, P., & Rolston, D. E. (1999). Modeling
521 diffusion and reaction in soils: 9. The Buckingham-Burdine-Campbell equation for gas
522 diffusivity in undisturbed soil. *Soil Science*, 164(2), 75.
- 523 NEON. (2024a). *Barometric pressure (DP1.00004.001)*. National Ecological Observatory
524 Network (NEON). <https://doi.org/10.48443/RT4V-KZ04>
- 525 NEON. (2024b). *Soil CO₂ concentration (DP1.00095.001)*. National Ecological Observatory
526 Network (NEON). <https://doi.org/10.48443/E7GR-6G94>
- 527 NEON. (2024c). *Soil physical and chemical properties, Megapit (DP1.00096.001)*. National
528 Ecological Observatory Network (NEON). <https://doi.org/10.48443/S6ND-Q840>
- 529 NEON. (2024d). *Soil temperature (DP1.00041.001)*. National Ecological Observatory Network
530 (NEON). <https://doi.org/10.48443/Q24X-PW21>
- 531 NEON. (2024e). *Soil water content and water salinity (DP1.00094.001)*. National Ecological
532 Observatory Network (NEON). <https://doi.org/10.48443/A8VY-Y813>
- 533 Norman, J. M., Kucharik, C. J., Gower, S. T., Baldocchi, D. D., Crill, P. M., Rayment,
534 M., Savage, K., & Striegl, R. G. (1997). A comparison of six methods for measuring
535 soil-surface carbon dioxide fluxes. *Journal of Geophysical Research: Atmospheres*, 102(D24),
536 28771–28777. <https://doi.org/10.1029/97JD01440>
- 537 Pedersen, A. R. (2024). *HMR: Flux Estimation with Static Chamber Data*.
- 538 Phillips, C. L., Bond-Lamberty, B., Desai, A. R., Lavoie, M., Risk, D., Tang, J., Todd-Brown,
539 K., & Vargas, R. (2017). The value of soil respiration measurements for interpreting and

- 540 modeling terrestrial carbon cycling. *Plant and Soil*, 413(1), 1–25. <https://doi.org/10.1007/s11104-016-3084-x>
- 541
- 542 Raftery, A. E., Gneiting, T., Balabdaoui, F., & Polakowski, M. (2005). *Using Bayesian Model*
543 *Averaging to Calibrate Forecast Ensembles*. <https://doi.org/10.1175/MWR2906.1>
- 544 Rheault, K., Christiansen, J. R., & Larsen, K. S. (2024). goFlux: A user-friendly way to
545 calculate GHG fluxes yourself, regardless of user experience. *Journal of Open Source*
546 *Software*, 9(96), 6393. <https://doi.org/10.21105/joss.06393>
- 547 Sallam, A., Jury, W. A., & Letey, J. (1984). Measurement of Gas Diffusion Coefficient under
548 Relatively Low Air-filled Porosity. *Soil Science Society of America Journal*, 48(1), 3–6.
549 <https://doi.org/10.2136/sssaj1984.03615995004800010001x>
- 550 Shao, J., Zhou, X., Luo, Y., Li, B., Aurela, M., Billesbach, D., Blanken, P. D., Bracho, R.,
551 Chen, J., Fischer, M., Fu, Y., Gu, L., Han, S., He, Y., Kolb, T., Li, Y., Nagy, Z., Niu, S.,
552 Oechel, W. C., ... Zhang, J. (2015). Biotic and climatic controls on interannual variability
553 in carbon fluxes across terrestrial ecosystems. *Agricultural and Forest Meteorology*, 205,
554 11–22. <https://doi.org/10.1016/j.agrformet.2015.02.007>
- 555 Shao, P., Zeng, X., Moore, D. J. P., & Zeng, X. (2013). Soil microbial respiration from
556 observations and Earth System Models. *Environmental Research Letters*, 8(3), 034034.
557 <https://doi.org/10.1088/1748-9326/8/3/034034>
- 558 Sihi, D., Gerber, S., Inglett, P. W., & Inglett, K. S. (2016). Comparing models of microbial–
559 substrate interactions and their response to warming. *Biogeosciences*, 13(6), 1733–1752.
560 <https://doi.org/10.5194/bg-13-1733-2016>
- 561 Tang, J., Baldocchi, D. D., Qi, Y., & Xu, L. (2003). Assessing soil CO₂ efflux using continuous
562 measurements of CO₂ profiles in soils with small solid-state sensors. *Agricultural and Forest*
563 *Meteorology*, 118(3), 207–220. [https://doi.org/10.1016/S0168-1923\(03\)00112-6](https://doi.org/10.1016/S0168-1923(03)00112-6)
- 564 Tang, J., Misson, L., Gershenson, A., Cheng, W., & Goldstein, A. H. (2005). Continuous
565 measurements of soil respiration with and without roots in a ponderosa pine plantation

- 566 in the Sierra Nevada Mountains. *Agricultural and Forest Meteorology*, 132(3), 212–227.
- 567 <https://doi.org/10.1016/j.agrformet.2005.07.011>
- 568 Taylor, J. R. (2022). *An Introduction to Error Analysis: The Study of Uncertainties in Physical*
569 *Measurements, Third Edition* (3rd ed.). University Science Press.
- 570 Wilson, S. J., Bond-Lamberty, B., Noyce, G., Bittencourt Peixoto, R., & Megonigal, J. P.
571 (2024). Fluxfinder: An R Package for Reproducible Calculation and Initial Processing
572 of Greenhouse Gas Fluxes From Static Chamber Measurements. *Journal of Geophysical*
573 *Research: Biogeosciences*, 129(11), e2024JG008208. <https://doi.org/10.1029/2024JG008208>
- 574 Yan, Z., Bond-Lamberty, B., Todd-Brown, K. E., Bailey, V. L., Li, S., Liu, C., & Liu, C. (2018).
575 A moisture function of soil heterotrophic respiration that incorporates microscale processes.
576 *Nature Communications*, 9(1), 2562. <https://doi.org/10.1038/s41467-018-04971-6>
- 577 Yan, Z., Liu, C., Todd-Brown, K. E., Liu, Y., Bond-Lamberty, B., & Bailey, V. L. (2016).
578 Pore-scale investigation on the response of heterotrophic respiration to moisture conditions
579 in heterogeneous soils. *Biogeochemistry*, 131(1), 121–134. <https://doi.org/10.1007/s10533-016-0270-0>
- 580 Zhang, R., Kim, S., Kim, H., Fang, B., Sharma, A., & Lakshmi, V. (2023). Temporal Gap-Filling
581 of 12-Hourly SMAP Soil Moisture Over the CONUS Using Water Balance Budgeting. *Water*
582 *Resources Research*, 59(12), e2023WR034457. <https://doi.org/10.1029/2023WR034457>
- 583 Zhao, J. (2019). FluxCalR: A R package for calculating CO₂ and CH₄ fluxes from static
584 chambers. *Journal of Open Source Software*, 4(43), 1751. <https://doi.org/10.21105/joss.01751>
- 585 Zobitz, J., Ayres, E., O'Rourke, K., Werbin, Z., Lee, L., Abdi, R., Mehmeti, D., & Xiong, L.
586 (2024). *neonSoilFlux: Compute Soil Carbon Fluxes for the National Ecological Observatory*
587 *Network Sites*.